Electrochemical oxygen reduction to hydrogen peroxide at practical rates in strong acidic media

Xiao Zhang [1,5✉], Xunhua Zhao [2,5], Peng Zhu [1], Zachary Adler [1], Zhen-Yu Wu [1], Yuanyue Liu [2✉] & Haotian Wang [1,3,4✉]

Electrochemical oxygen reduction to hydrogen peroxide (H_2O_2) in acidic media, especially in proton exchange membrane (PEM) electrode assembly reactors, suffers from low selectivity and the lack of low-cost catalysts. Here we present a cation-regulated interfacial engineering approach to promote the H_2O_2 selectivity (over 80%) under industrial-relevant generation rates (over 400 mA cm^{-2}) in strong acidic media using just carbon black catalyst and a small number of alkali metal cations, representing a 25-fold improvement compared to that without cation additives. Our density functional theory simulation suggests a "shielding effect" of alkali metal cations which squeeze away the catalyst/electrolyte interfacial protons and thus prevent further reduction of generated H_2O_2 to water. A double-PEM solid electrolyte reactor was further developed to realize a continuous, selective (~90%) and stable (over 500 hours) generation of H_2O_2 via implementing this cation effect for practical applications.

[1] Department of Chemical and Biomolecular Engineering, Rice University, Houston, TX 77005, USA. [2] Texas Materials Institute and Department of Mechanical Engineering, The University of Texas at Austin, Austin, TX 78712, USA. [3] Department of Chemistry, Rice University, Houston, TX 77005, USA. [4] Department of Materials Science and NanoEngineering, Rice University, Houston, TX 77005, USA. [5]These authors contributed equally: Xiao Zhang, Xunhua Zhao. ✉email: xiao1.zhang@polyu.edu.hk;yuanyue.liu@austin.utexas.edu; htwang@rice.edu

Hydrogen peroxide (H_2O_2) is ranked as one of the top 10 most energy-intensive chemicals in the chemical manufacturing bandwidth study by the Advanced Manufacturing Office in Department of Energy[1]. It is currently manufactured industrially by the energy- and waste-intensive anthraquinone cycling process[2–4], which consumes a primary current typical energy of ~13,000 Btu/lb (8.1 kWh/kg) without taking into account the H_2/O_2 feedstocks[1]. Electrochemical synthesis of H_2O_2 via the $2e^-$ oxygen reduction reaction ($2e^-$–ORR), where the O_2 molecule is electrochemically reduced to H_2O_2 via a two-electron ($2e^-$) pathway, provides a promising energy-efficient and low-waste alternative[2–7]. Recent efforts have been mostly focused on developing catalysts in alkaline solutions, in which small overpotential and high selectivity of $2e^-$–ORR toward H_2O_2 have been comparatively easy to achieve on low-cost materials such as carbon[8–18]. However, in alkaline solutions, H_2O_2 is deprotonated ($pK_a > 11$) and easily degraded[19]. Moreover, for practical electrolyzers such as membrane electrode assembly (MEA), catalysts developed in alkaline solutions need to be applied on an anion exchange membrane (AEM), which is typically not as stable as its counterpart of proton exchange membrane (PEM), e.g., Nafion[4], especially operated under air. In addition, with stronger oxidation ability in acid, the acidic H_2O_2 solution shows a wider range of applications and greater demand[6,20], which strongly motivates studies in high-performance electrochemical generation of H_2O_2 in acidic media.

Till so far, there are only a few known noble metal catalysts, including Pt- and Pd-based catalysts, demonstrated to be selective and stable for $2e^-$–ORR in strong acids[21–24], but their high cost and toxicity of heavy metals (in the case of PtHg alloy[22,23]) could limit their applications in large-scale H_2O_2 generation. Some low-cost catalysts such as carbon materials may also show good H_2O_2 selectivity in acids within small overpotential and small current density regions (typically less than $10\,mA\,cm^{-2}$)[25–29], but their H_2O_2 selectivity and stability were dramatically dropped when an industrial-relevant current was reached[5,27,30]. In acidic media, carbon catalysts present sluggish ORR kinetics and typically require a large overpotential (>300 mV) to initiate the ORR reaction, and consequently, a large negative cathodic overpotential is required to deliver a high current density[26–29]. While the carbon surface might intrinsically prefer a $2e^-$–ORR pathway due to their relatively weak binding with oxygen intermediates as demonstrated by several previous studies[26,27,30,31], such negative overpotential could further push the ORR reaction all the way down to H_2O with significantly decreased H_2O_2 selectivity and production rate especially in acids. This is because under negative potentials in acids, the catalyst surface accumulates concentrated protons that are prone to further reduce the locally generated H_2O_2 molecules to H_2O ($H_2O_2 + 2e^- + 2H^+ = 2H_2O$). Therefore, diluting the local proton concentration and minimizing the electrochemical dissociation of as-produced H_2O_2 to H_2O could be one promising strategy for resolving this H_2O_2 selectivity-activity dilemma, and delivering industrial-relevant H_2O_2 production rate in acidic solution while maintaining good H_2O_2 selectivity[32,33] (Fig. 1).

Results

The alkali metal cation effect on acidic H_2O_2 generation in flow cell.
We first employed a standard three-electrode flow cell reactor to investigate the cation effect towards H_2O_2 generation in acid (Fig. S1), allowing to evaluate our hypothesis in a more practical environment and produce H_2O_2 under higher current densities compared to the traditional RRDE setup (Supplementary Note 1, Fig. 2a). The commercially available carbon black catalyst (BP2000) with a high surface area was used as a model ORR catalyst in this study (Fig. S2). Its intrinsic H_2O_2 activity and
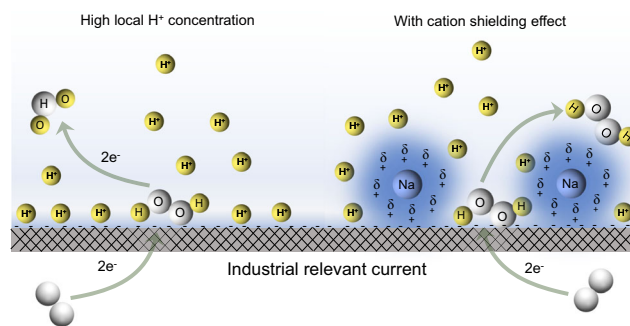
Fig. 1 Schematic illustration of $2e^-$–ORR toward H_2O_2 in acid with/without Na^+ under industrial-relevant current. Here we report a cation-regulated catalyst/electrolyte interface to promote electrochemical O_2 reduction to H_2O_2 in acids with high-selectivity and industrial-relevant production rates. By adding only a small amount of alkali metal ions into the acidic electrolyte, which barely affects the solution's pH, we demonstrated a dramatic improvement in H_2O_2 selectivity and activity especially under large ORR current densities across different catalysts. Our molecular dynamic simulations suggest that the solvated alkali metal cations, compared to concentrated protons in acids, could preferentially be attracted to the catalyst/electrolyte interface and squeeze out local protons during the reaction, suppressing the further reduction of as-generated H_2O_2 to H_2O (Fig. 1). Using commercial carbon black catalysts with 10 mM Na_2SO_4 as an additive, the H_2O_2 Faradaic efficiency (FE) can reach over 80% under a significant current of $400\,mA\,cm^{-2}$ in 0.1 M H_2SO_4, representing a 25-fold improvement compared to the case without Na^+ additive where negligible H_2O_2 was produced (<5% FE). Based on this cation promotion concept, a double-PEM-based solid electrolyte (SE) reactor was developed for a continuous generation of H_2O_2 with high FE (~90%) and good stability (over 500 h) for practical applications in the future.

selectivity were first evaluated in 0.1 M H_2SO_4 electrolyte (pH = 0.96) (Fig. 2b, c). We observed that while the H_2O_2 FE of carbon black catalyst in acid remained relatively good (~70%) under small current regions, it started to decrease dramatically once the current density is over $100\,mA\,cm^{-2}$ with very negative applied potentials (Fig. 2c). Under $200\,mA\,cm^{-2}$, the carbon black catalyst can only deliver a 35% H_2O_2 FE and the majority of electrons were directed towards H_2O instead (Fig. 2c). The decreased FE is as expected, because under such a negative potential of −0.89 V versus reversible hydrogen electrode (vs. RHE) needed to drive this high current, even if the catalyst prefers to reduce O_2 to H_2O_2 in its first place, those generated H_2O_2 at the electrode surface could be easily further reduced to H_2O coupling two electrons and two local protons. Please be noted here that, under each current density, its corresponding H_2O_2 FE was measured within 8 min of operation. With a longer time of electrolysis, the H_2O_2 FE could be further dropped (as shown in the stability test in Fig. 3g). After introducing a trace amount of Na^+ additive (5 mM Na_2SO_4) into the acidic electrolyte, while the ORR activity did not show that much difference (Fig. 2b), the H_2O_2 FE was significantly improved especially under high current densities. As shown in Fig. 2c, in the potential range of the ORR onset, the impact of Na^+ (5 mM Na_2SO_4) toward H_2O_2 is negligible; while in the range of large overpotentials at high current densities, the small amount of Na^+ helped the carbon black catalyst to hold a high H_2O_2 FE plateau of over 80% until $200\,mA\,cm^{-2}$, suggesting a more than doubled FE compared to that in pure acid (Fig. 2c).

The measured trends of H_2O_2 FE show that the promotion effect of Na^+ is more pronounced at high current density toward H_2O_2 formation. We understand that Na^+ and protons are both positively charged ions and will be attracted towards the ORR
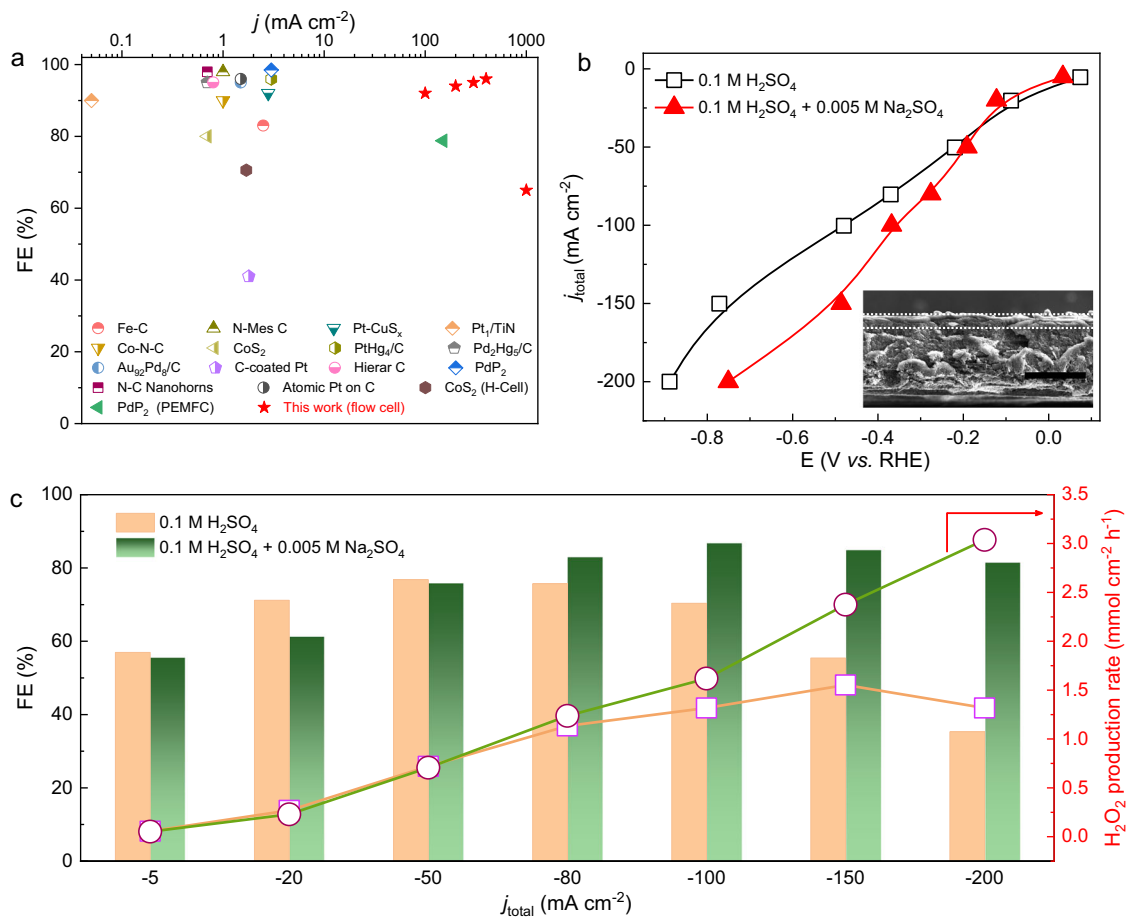
Fig. 2 Na⁺ effects toward acidic H₂O₂ generation through 2e⁻–ORR. a Reported current densities and Faradaic efficiencies (FEs) for 2e⁻–ORR toward H₂O₂ in acid in literatures (listed in Table S1). **b** Effect of 0.005 M Na₂SO₄ on the total activity over carbon catalysts BP2000 in a flow cell. The cell voltages were 85% iR compensated. The inset is the cross-section SEM image of the electrode. The scale bar is 200 μm. **c** The comparison of H₂O₂ FE and production rate over carbon catalyst BP2000 with/without 0.005 M Na₂SO₄ in a flow cell. The Na⁺ serves as a promoter for the production of H₂O₂ through 2e⁻–ORR. The H₂O₂ FE and production rate are both increased, especially at the high current range.

catalyst surface to form the electrochemical double layer under negative potentials[34]. We would assume that, Na^+ ions could be more competitive than protons to be aligned along the electro-chemical double layer, which dramatically reduces the local proton concentration and thus protects the generated H_2O_2 from further reductions coupling protons and electrons (discussed in the following sections in detail). To further amplify the cation effect and drive the O_2-to-H_2O_2 production at even higher current densities in acid (>200 mA cm⁻²), we gradually increased the Na^+ cation concentration in the electrolyte. As shown in Fig. 3a, the overall current density, as well as the H_2O_2 FE gradually increases with increased Na^+ concentrations. In general, a higher con-centration of Na^+ can maintain larger 2e⁻–ORR currents without sacrificing the H_2O_2 selectivity. With only 0.01 M Na_2SO_4 in 0.1 M H_2SO_4, the FE of H_2O_2 can reach 83% at 400 mA cm⁻² (Fig. 3b), representing a 25-fold improvement compared to that in pure acids without Na^+ (H_2O_2 FE only 3.3%). Along with the increased H_2O_2 FE, the improvement of the H_2O_2 production rate was also obvious at high current densities (Fig. 3c). For example, the production rate of 6.21 mmol cm⁻² h⁻¹ H_2O_2 (partial current of 332 mA cm⁻²) was achieved under the current density of 400 mA cm⁻², much higher than that in pure H_2SO_4 acid (only 0.245 mmol cm⁻² h⁻¹). The production rate can be further enhanced by providing more Na^+ cations (the production rate of 6.52 mmol cm⁻² h⁻¹ was achieved at 400 mA cm⁻² and the

maximum FE can be up to 94% at 150 mA cm⁻² by using 0.05 M Na_2SO_4 as additive). Further increasing the concentration of Na^+ cations could continually push up the H_2O_2 FE to higher values at high current densities (Fig. S3). It is important to note here that the electrolyte pH did not show obvious change and stayed around pH 1 after these Na_2SO_4 additives, ranging from 0.96 (0.1 M H_2SO_4), 0.96 (0.1 M H_2SO_4 + 0.005 M Na_2SO_4), 0.98 (0.1 M H_2SO_4 + 0.01 M Na_2SO_4) to 1.04 (0.1 M H_2SO_4 + 0.05 M Na_2SO_4). To fully exclude the pH effect of the bulk solution (even though the change is quite small), the pH value of 0.1 M H_2SO_4 + 0.1 M Na_2SO_4 (pH = 1.13) was adjusted to be the same as that of 0.1 M H_2SO_4 (pH = 0.96) by adding more sulfuric acid. As shown in Fig. S4 and S5, the H_2O_2 FE in both electrolytes with Na^+ additives (before and after pH tuning) showed very similar trend in all current ranges, indicating the Na^+ cations dominate the H_2O_2 generation process and the small pH differences of electrolytes have negligible influence on the production rate or H_2O_2 FE. With 0.1 M Na_2SO_4 as an additive in 0.2 M H_2SO_4 solution (pH = 0.76), we were able to produce H_2O_2 at the current density of 1 A cm⁻² with a FE of more than 65% (Fig. S6). The H_2O_2 partial currents of up to 650 mA cm⁻² were achieved, and high FEs were maintained, better than the highest O_2-to-H_2O_2 conversion rates reported. At even lower pH electrolyte, i.e., 1 M H_2SO_4 solution (PH~0), similar trends were also observed (Fig. S7), indicating the general phenomenon of cation promotion effect toward H_2O_2 production through ORR.
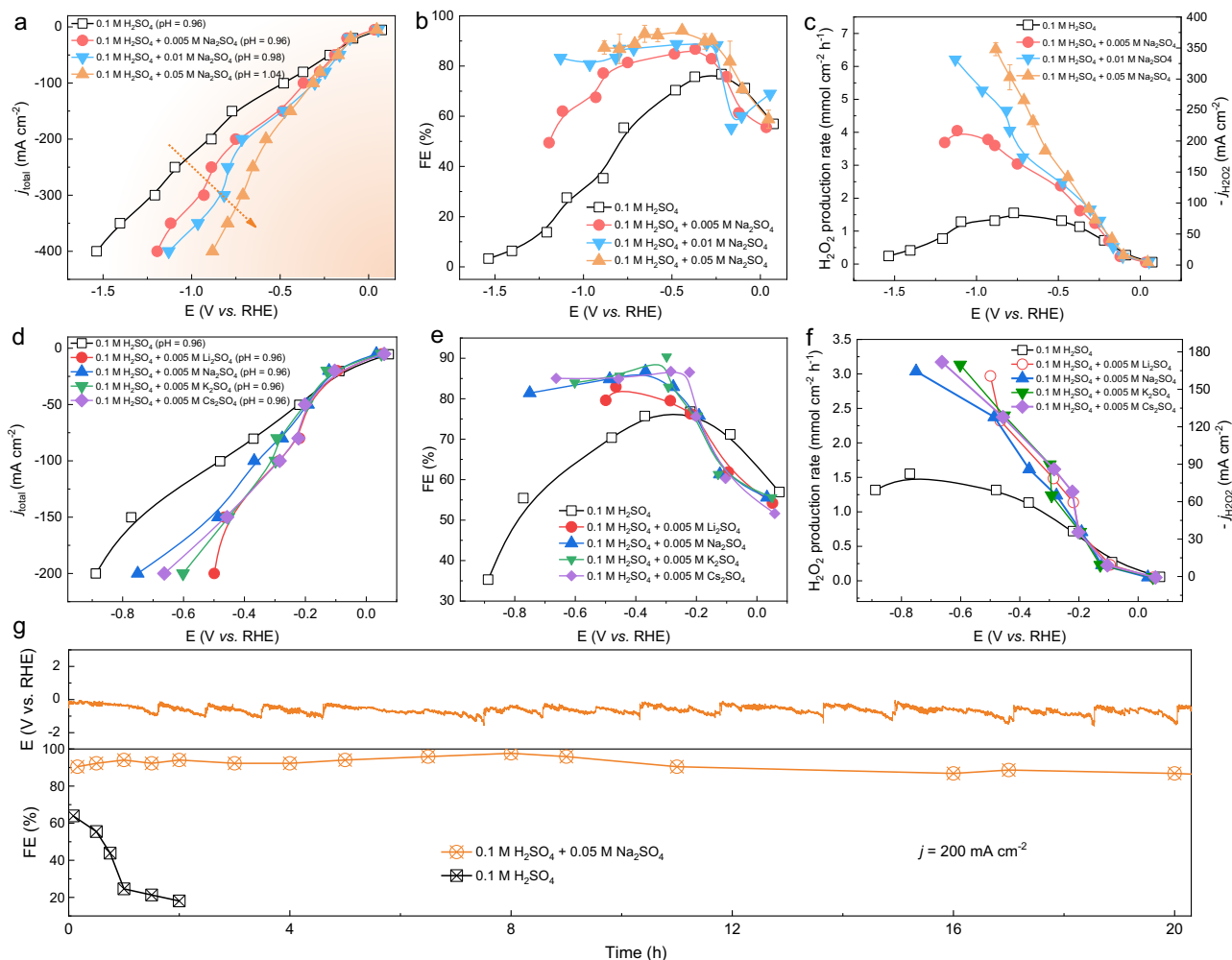
Fig. 3 The effect of alkali metal cation concentration and species on electrosynthesis of H₂O₂ through 2e⁻–ORR. a The I-V curve of ORR with different concentrations of cations (from 0 to 0.05 M Na₂SO₄) in a flow cell. **b** The corresponding FEs and (**c**) production rates and partial current of H₂O₂ products under different cell voltages. With the increase of cation concentration, the H₂O₂ FE and production rate continuously increase at high current densities. The error bars represent two independent tests. **d** The I-V curve of ORR in 0.1 M H₂SO₄ containing different types of cations (0.005 M X₂SO₄, X = Li⁺, Na⁺, K⁺, Cs⁺) in a flow electrolyte cell. **e** The corresponding FEs and (**f**) production rates and partial current of H₂O₂ products under different cell voltages. **g** Chronopotentiometry stability comparison of carbon catalysts BP2000 with/without cations by holding 200 mA·cm⁻² current density for 20 h in a flow cell for continuous electrolysis. The geometric area of the flow field at the cathode in the flow cell is 1 cm².

The low threshold of the alkali metal cation concentration towards promoting H₂O₂ generation puts forward new requirements for the purity of the electrolyte during ORR to H₂O₂ tests in acids. For the traditional electrolytic ORR process, the Na₂SO₄ is widely used as the anolyte to balance the electrochemical reaction. However, even far away from the cathode side and separated by ion exchange membranes, we found that the Na⁺ in the anolyte can still penetrate the PEM and move to the cathode chamber, and thus significantly improve the H₂O₂ FE of ORR at the cathode (Fig. S8). Therefore, it is highly recommended to perform the ORR reaction using the same acidic electrolyte to avoid any cross-over cation contaminations which could significantly improve H₂O₂ performance in acids.

The promotion effect is not only limited to the Na⁺. The H₂O₂ production rate can also be enhanced by using other alkali metal ions. Figure 3d shows the I-V curves for four different alkali metal cations in each sulfuric acid electrolyte with a concentration of 0.01 M (0.005 M X₂SO₄, X = Li, Na, K, Cs). As compared with the pure H₂SO₄ electrolyte, while the ORR activities were slightly improved, significant improvements in H₂O₂ FE were observed for all the cations (Fig. 3d–f). The FE and production rates of

H₂O₂ are relatively unaffected by the size of the alkali metal cations in the electrolyte. As differences in total current density exist for electrolytes containing different cations, the H₂O₂ production rate provides a better representation of trends in product formation rates than FEs. As shown in Fig. 3f, with 0.005 M X₂SO₄ as the additive, all the alkali metal cations are able to drive the O₂-to-H₂O₂ reaction efficiently with high production rates, and the differences induced by different cations are relatively marginal. Nevertheless, we find that the promotion effect is only limited to IA alkali metal cations (such as Li⁺, Na⁺, K⁺, Cs⁺), while the other cations (including the IIA cations such as Mg²⁺, Ca²⁺ and IIIA cations such as Al³⁺) decrease the H₂O₂ FE dramatically. This might due to the local environment change from acid to alkaline induced by the cation additives during ORR (will discuss the details in the simulation part). The alkaline local environment could induce the formation of solid metal hydroxide on the catalyst surface and block the ORR reaction, decreasing the H₂O₂ FE and production rate (Fig. S9).

It was also exciting to find out that the cation additives not only promote the H₂O₂ selectivity but also improve the long-term operation stability, which is another important target for practical
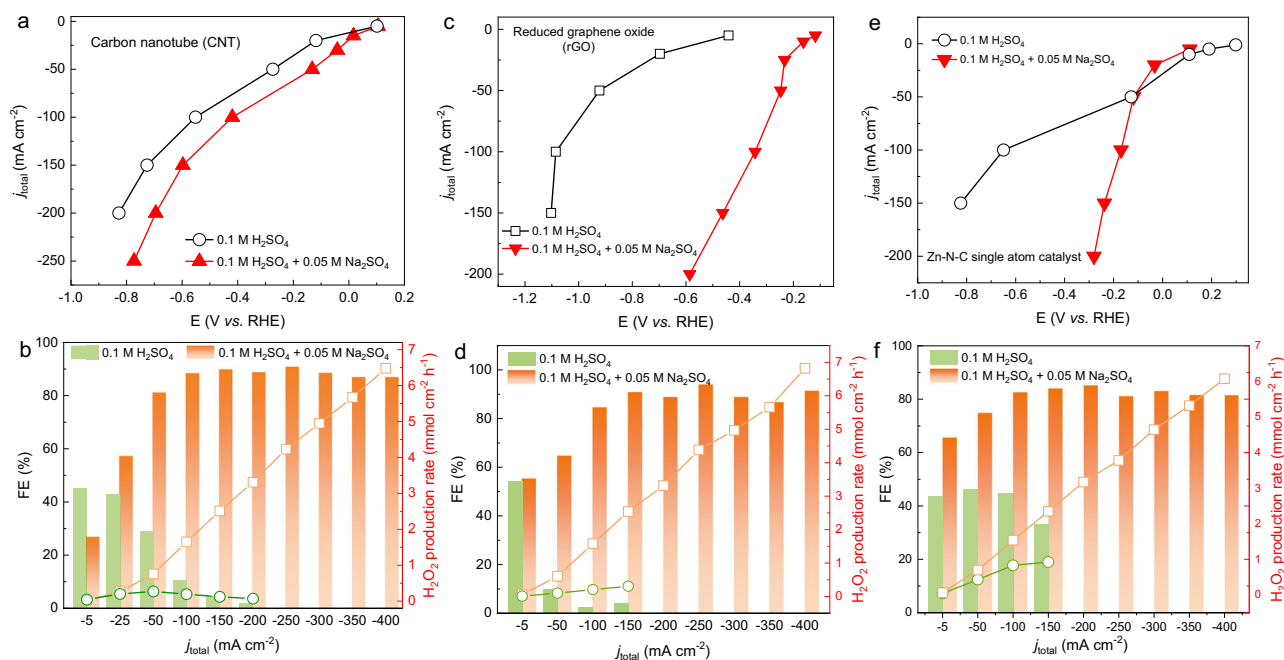
Fig. 4 The Na$^+$ effect towards electrochemical production of H$_2$O$_2$ on diverse carbon-based electrocatalysts. The I-V curve of ORR in 0.1 M H$_2$SO$_4$ or 0.1 H$_2$SO$_4$ + 0.05 M Na$_2$SO$_4$ electrolytes using (**a**) CNT, **c** rGO, **e** Zn-N-C single-atom catalysts. The corresponding FEs and production rates of H$_2$O$_2$ in 0.1 M H$_2$SO$_4$ or 0.1 H$_2$SO$_4$ + 0.05 M Na$_2$SO$_4$ electrolytes using (**b**) CNT, **d** rGO, **f** Zn-N-C single-atom catalysts.

production of H$_2$O$_2$. Figure 3g shows the comparison of H$_2$O$_2$ FE at 200 mA/cm^2 ORR current as a function of operation time in the flow cell. In pure acidic electrolyte, the H$_2$O$_2$ FE rapidly dropped to less than 10% within 2 h. As a sharp contrast, with the presence of Na$^+$ cations, the potential and H$_2$O$_2$ FE showed negligible changes for over 20 h. We suppose the improved activity and stability are induced by the alkalization of the local environment induced by the cation additives during ORR. During the ORR process, the solvated alkali metal cations, compared to concentrated protons in acids, could preferentially be attracted to the catalyst/electrolyte interface, which gives rise to a local alkaline environment (will discuss the details in the simulation part). At alkaline conditions, the carbon-based catalyst typically shows higher activity and better stability compared to acidic conditions[8–10]. We then found this cation promotion effect has broad applicability to different catalysts and acidic electrolytes. With a small amount of Na$_2$SO$_4$ as the additive in 0.1 M H$_2$SO$_4$ (Fig. 4), high H$_2$O$_2$ FE under high production rates can be achieved on various carbon catalysts including carbon nanotube (CNT), reduced graphene oxide (rGO), XC-72, and the carbon-based single-atom catalysts (e.g., Zn-N-C). This promotion effect is independent of the catalyst structures, surface morphology or surface area (Figs. S10–S12). In addition, this cation impact on 2e$^-$–ORR also applies to other acidic electrolytes such as HClO$_4$, and the Na$^+$ sources can also come from other salts such as NaHSO$_4$ (Figs. S13, S14).

Mechanistic understanding of the cation effect on H$_2$O$_2$ selectivity. To further explore our aforementioned hypothesis and understand the cation effects on 2e$^-$–ORR selectivity, we carried out constant-potential *ab*-initio molecular dynamics (AIMD) simulations[35] based on DFT. In the simulations, we use a typical potential V$_{RHE}$ (potential relative to RHE) = −1 V at which the cation effect is most prominent. The hydrogen evolution reaction was not considered because only a trace amount of H$_2$ byproduct (from H$_2$ evolution at large overpotentials) was detected from the cathode side (Fig. S15). We consider the

acid condition and use pH = 0 in our simulations. Since alkali metal cations are not likely to directly participate in ORR, we explore two aspects of the cation effects: (1) how alkali metal cations affect the distribution of the protons, (2) how the redistribution of protons will influence the selectivity of O$_2$ reduction to H$_2$O$_2$. For the first question, we adopted a model with relatively thick water layers (equivalent to 6 ice layers) on (6 × 6) periodic graphene (Fig. S16), and then put a certain number of cations/protons to represent the electrode environment under the lower potential like V$_{RHE}$ = −1 V. For the second question, we use a thinner model (~4 ice layers) with single-vacancy to represent the reaction site, and then use slow-growth method[36] to evaluate the reaction barrier under different conditions). The details of the simulations can be found in the experiment section in supporting information (SI).

As shown in Fig. 5a, b, both Na$^+$ cations drift towards the surface in molecular dynamics. This is not unexpected considering that under the low potential V$_{RHE}$ = − 1 V, the surface is charged by ~3e$^-$. Such a fast drift may have two consequences: firstly, the local concentration of Na$^+$ can be much higher than that in the bulk; secondly, as a charge carrier that compensates the net charge of the substrate, Na$^+$ may compete with protons which is the major charge carrier in the acid electrolyte when Na$^+$ cations are not added. Indeed, as shown in Fig. S17, when Na$^+$ cations and protons co-exist near the interface, the cations compete with the protons by repelling the proton away from the surface. After 3 picoseconds of AIMD, both cations stay ~4.5 Å from the surface, while the protons end at ~8 Å from the surface. These results clearly suggest that the cations, which can be enriched by the attraction of the negatively charged surface, can strongly repel the local protons, and thus dramatically reduce the local proton concentrations.

Then we consider how the selectivity of the 2e$^-$–ORR is affected by the presence of Na$^+$ cations and the reduced local proton concentrations. We understand that carbon catalysts typically bind oxygen intermediates weakly and thus present an intrinsic selectivity towards H$_2$O$_2$, which can be seen from our above experimental results (high H$_2$O$_2$ selectivity under low currents in Fig. 2c) as well as
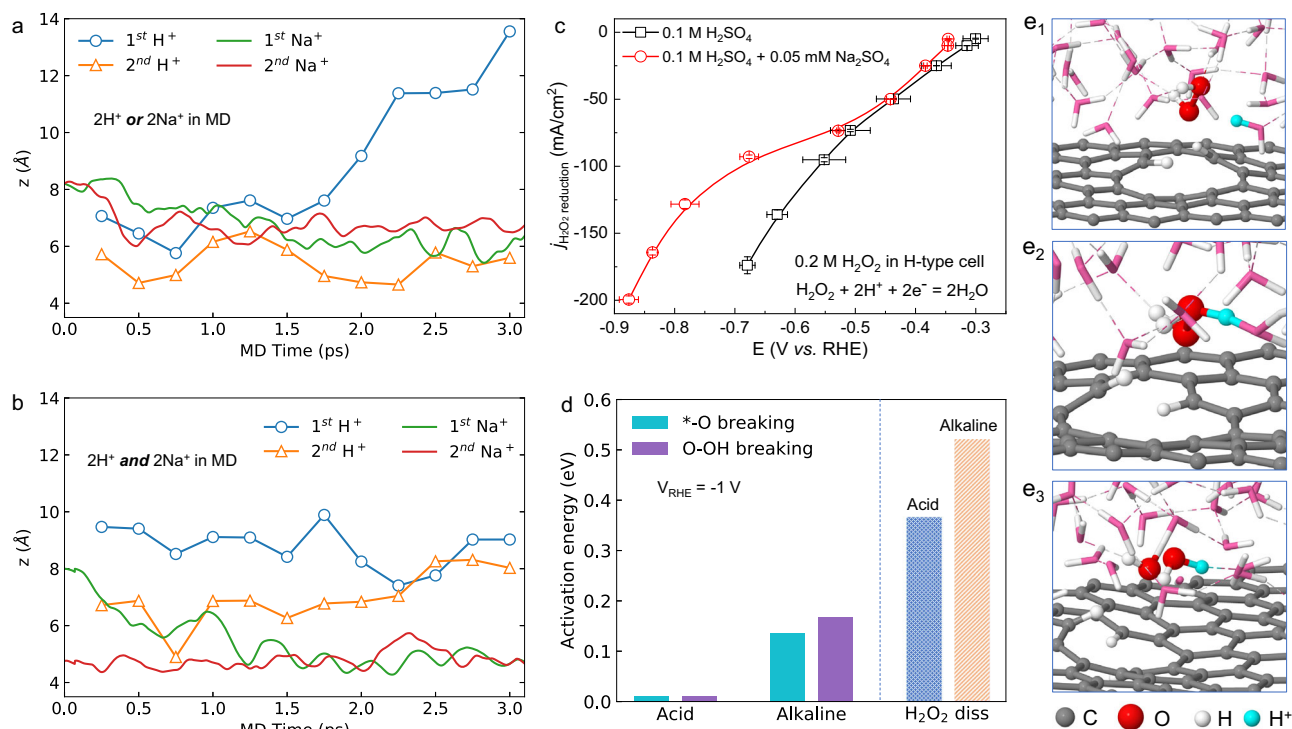
Fig. 5 Electrochemical H_2O_2 dissociation and simulation of the Na^+ effect at the local environment of catalyst surface. a, b Evolution of the position (surface normal direction "z") of Na^+ ions (and/or) H^+ after positioning them in the water layers; **c** the partial current of electrochemical H_2O_2 dissociation as a function of the voltage by using 0.1 M H_2SO_4 or 0.1 M H_2SO_4 + 0.05 M Na_2SO_4 electrolyte in H-type cell. The measured potentials were manually 100% compensated. The error bars represent two independent tests. **d** activation energies calculated through constant potential molecular dynamics (see SI for more details). **e_1–e_3,** Initial state, transition state and final state of the H_2O_2 decomposition in neutral solution. C: grey; O: red; H: white; Proton: cyan.

previous reports[9,11]. The catalyst's H_2O_2 selectivity starts to drop under significant overpotentials to deliver large currents in pure acids, where two possible reaction mechanisms could play a role in guiding the reaction towards the $4e^-$ pathway of H_2O. One possibility is that, while the catalyst still produced H_2O_2 selectively in the first place, those locally generated H_2O_2 under such negative potentials could be further reduced to H_2O coupling electrons and protons ($H_2O_2 + 2e^- + 2H^+ = 2H_2O$), resulting in a low apparent H_2O_2 selectivity. In this case, as the Na^+ cation additives can effectively screen away local protons, the further dissociation of generated H_2O_2 can be depressed, resulting in better H_2O_2 selectivity. This "cation protection" of as-formed H_2O_2 can be validated by performing the electrochemical reduction of H_2O_2 in both pure and Na^+-containing acidic electrolytes (Figs. S19–21, Fig. 5c). As shown in Fig. 5c, the H_2O_2 reduction activity was greatly suppressed, especially under large overpotentials, when Na^+ was added, suggesting that the introduction of cations can greatly inhibit the H_2O_2 dissociation to H_2O under reductive potential environments. Please be noted here that the only possible side reaction, the hydrogen evolution reaction, was also taken into consideration when measuring the H_2O_2 reduction currents (Fig. S15). This suppression effect can be further validated from our simulation results. Clearly, as shown in Fig. 5d, the absence of protons increases the H_2O_2 decomposition barrier to 0.519 eV, 0.156 eV higher than that when a proton is present. The initial state, transition state and final state of H_2O_2 decomposition are shown in Fig. 5e and S17. As the O-O bond elongates, the proton attaches to one of the O in H_2O_2 and forms a HO-OH_2 complex at transition state and eventually forms OH^- and H_2O. This process clearly shows how the proton promotes H_2O_2 decomposition, explaining the reason why cations could prevent the further reduction of as-synthesized H_2O_2 by screening out local protons.

Another possible factor for improved H_2O_2 selectivity is that the cations could suppress the dissociation process of peroxide intermediate ($*OOH$) during ORR due to local proton depletion. To explore this hypothesis, we further used a slow-growth approach based on AIMD to evaluate the reaction barriers of both $2e^-$ and $4e^-$ paths under different proton concentration conditions. As displayed in Fig. 5d, when a proton is present, both the $2e^-$ path and $4e^-$ paths have an extremely low barrier and take place spontaneously at 300 K. In contrast, the absence of protons increases the $*$-O breaking ($2e^-$ path) barrier to 0.136 eV, in comparison to 0.167 eV for O-OH breaking ($4e^-$ path), suggesting $2e^-$ pathway being favorable by $\exp((0.167-0.136)k_BT) = 3.36$ times than the $4e^-$ pathway and thus enhanced H_2O_2 selectivity. Therefore, the local absence of protons, a result of cation accumulation near the surface, can strongly enhance the H_2O_2 selectivity in acids.

We also evaluate the effect of Mg^{2+} on the $2e^-$–ORR by replacing two Na^+ by one Mg^{2+}, and running the AIMD simulations similar to the case of Na^+ (Fig. 5b). As shown in Fig. S27, Mg^{2+} does not show the same effect as Na^+. This is likely due to two reasons: (1) Mg^{2+} is more efficiently screened as the Mg^{2+} bonds stronger with O of H_2O than the case of Na^+, which is evidenced by the significantly shorter distance between Mg and O (averaged distance $d_{Mg-O} = 2.05$ Å vs. $d_{Na-O} = 2.55$ Å); (2) the mole concentration of Mg^{2+} is only half of that of Na^+ in the electrical double layer and the electrostatic repelling decays in the form of $1/r$, so there is more "screened" space for H^+ in the electrical double layer.

Practical generation of H_2O_2 using cation exchange membrane solid electrolyte reactor. Obtaining good H_2O_2 selectivity and activity in acidic ORR is a prerequisite for practical implementations of membrane electrode assembly (MEA) reactor using

reliable and well-established PEM such as Nafion (sulfonated tetrafluoroethylene based fluoropolymer-copolymer membrane). However, till so far, only noble metal catalysts such as PtHg, PdHg or PtP_2 nanocrystals could deliver reasonable H_2O_2 selectivity and stability in proton exchange MEA device[22,23,37]. This observed notable promotion effect of cations on low-cost and non-toxic carbon catalysts in acidic H_2O_2 generation therefore provides us with a great opportunity to deliver practical H_2O_2 activity, selectivity, and stability. Our basic assumption is that, as the alkali metal cations can move across the PEM, they may help to regulate the local environment of the catalyst/membrane interface for better H_2O_2 activity and selectivity. To explore how to successfully make use of this cation tuning effect, we first evaluated its applicability in a traditional PEM-MEA cell configuration (Figs. S22–S24). First, it is well within our expectation that the traditional PEM-MEA cell using commercial carbon black catalyst with 0.1 M H_2SO_4 as the anolyte, presented negligible H_2O_2 selectivity, due to the high proton flux at the catalyst/membrane interface (Fig. S22). However, we found out that even with the addition of cations in acids (Fig. S23), or directly using Na_2SO_4 solution as the anolyte (Fig. S24), no obvious improvements were observed. This is because on the anode side, a significant number of protons will be generated locally at the catalyst/membrane interface during the oxygen evolution reaction and then immediately transported across the membrane to the cathode side, suppressing the possibility of Na^+ ion transportation from the bulk anolyte towards the cathode to regulate the interfacial environment of improved $2e^−$–ORR. The low H_2O_2 selectivity in PEM-MEA drove us to design a new cell configuration to employ this cation effect for continuous production of H_2O_2 in a practical way.

Instead of the traditional PEM-MEA cell design, here we developed a SE reactor with three chambers separated by two PEMs to fully implement this cation effect for high-performance H_2O_2 generation (Fig. 6a and Fig. S25). Specifically, the cathode (carbon black) and anode (IrO_2) of our device are catalyst-coated GDL electrodes, which were separated by a thin SE layer sandwiched by two identical PEMs (Nafion-117). The cathode side was continuously supplied with a mixture of O_2 stream and water flow for $2e^−$–ORR, while the anode side was circulated with H_2O for water oxidation. In the middle chamber, a SE layer consisting of porous polymer ion conductors was used to minimize the iR-drop between cathode and anode[38,39]. A dilute cation solution flows through this SE layer to introduce the cation effects on the cathode side $2e^−$–ORR. Please be noted here that without this SE layer, the cell voltage was significantly increased due to the increased cell resistance between the cathode and anode (Fig. S26). Under a negative reduction potential, the cations in the middle SE chamber are driven by the electrical field to penetrate the PEM toward the cathode surface and thus regulate the local environment at the catalyst/PEM interface to promote H_2O_2 generation (Supplementary Note 2 and Fig. S27). The H_2O_2 molecules formed at the cathode side are then efficiently brought out via the oxygen and DI water flow stream. Meanwhile, protons generated from water oxidation at the anode penetrate the righthand side PEM and move into the middle chamber to compensate for the charge.

The I–V curve of our 4-cm² three-chamber PEM SE cell flowing 0.03 M Na_2SO_4 solution in the middle layer is plotted in Fig. 6b. Of note that the concentration of Na_2SO_4 can be varied to higher values. Our target is to realize the high production rate of H_2O_2 while minimizing cations' consumption for practical demonstrations. Therefore, a 0.03 M Na_2SO_4 solution is adopted to regulate the interfacial environment of improved $2e^−$–ORR in our SE cell. A mixture of O_2 gas flow (180 sccm) and DI water flow (1.8 mL·min⁻¹) was supplied to the cathode. The flow of DI

water is to efficiently bring out the generated H_2O_2. By ramping up the overall current density, the cell voltage of the SE reactor gradually increased. The H_2O_2 FE remained over 85% across the entire cell voltage range, with a maximum of 96% at 5 and 20 mA cm⁻² (Fig. 6b), much higher than the traditional MEA cell configuration. In comparison, the reactor without alkali metal cations requires a higher potential to deliver and shows much lower H_2O_2 FE, practically at high current densities (Fig. S28). The crosse-over Na^+ from the middle SE layer to the cathode plays a key role in determining the H_2O_2 FE (Fig. S27).

The electrolysis stability is always one of the most important but challenging parts in practical applications. Benefiting from the stable material properties in carbon black and PEM as well as reliable cation effects, our SE cell with the double-PEM configuration presents excellent long-term stability in producing H_2O_2. The SE reactor stability was evaluated by holding a 50 mA·cm⁻² cell current density (200 mA total current). As shown in Fig. 6c and d, when supplying dilute Na^+ ions in the SE layer, a continuous generation of H_2O_2 solution on the cathode side can be stably operated for over 500 h with no degradations in product FE (~90%). As a sharp contrast, in the absence of cations, the H_2O_2 FE started with less than 60% and rapidly dropped to less than 10% in 6 h, which can even be recovered to ~90% when cations were later introduced (Fig. S29), clearly suggesting this prominent cation effect. The observation indicates that the carbon catalyst still works well, and this is not the reason for FE degradation. We suppose the FE degradation is because of the accumulation of local H^+ to high concentrations with the extension of reaction time, which accelerates the further reduction of H_2O_2 to H_2O and decrease the H_2O_2 selectivity.

A continuous supply of cation solutions in the SE layer could limit the device's real applications due to the following two reasons. First, it could result in a significant consumption of cations as most of them are flowing out of the SE layer and only part of them crossed to the cathode chamber. Second, the generated H_2O_2 solution in the cathode would be slightly alkaline due to the Na^+ ion crossover from the SE layer (resulting in slight acidity in the SE layer downstream flow). To further explore the high potential of our SE cell for practical uses, we operated the cell by circulating the cation solution from the SE layer into the cathode side, and then back to the SE layer for H_2O_2 accumulation. The outlet solution in the middle chamber was mixed with oxygen flow and supplied to the cathode to produce H_2O_2. Then the as-produced solution containing H_2O_2 and cations was cycled back into the middle chamber (Fig. 6e). By doing so we could continuously reuse the cations by circulating them back to the SE layer for a closed system without the need for a continuous cation stream supply. Also, the excessive $OH^−$ groups generated from the cathode would be neutralized by exactly the same number of excessive protons in the SE layer. Our target is to accumulate the H_2O_2 concentration to ~5000 ppm in a 250 mL solution (containing only 60 mM of Na^+) for each operation cycle via maintaining a 50 mA cm⁻² cell current. As shown in Fig. 6f, the H_2O_2 concentration continuously increased to ~5000 ppm in about 13 h. The cell can be operated for more than 200 h with negligible degradations. During this stability test, a total of 3.7 L 5000 ppm H_2O_2 solution was obtained. We also observed that, in each operation cycle the H_2O_2 FE slightly decreases with increased H_2O_2 concentration, which may be due to the H_2O_2 self-decomposition, further reductions on the cathode, and/or the crossover oxidation on the anode side. For each operation cycle, the H_2O_2 concentration can reach up to ~0.15 M, which is 5 times of the Na_2SO_4 additive in the final product. A higher concentration of H_2O_2 solutions can also be produced by extending the operation time while maintaining the current and FE. As a result, a high concentration of of 20,000 ppm
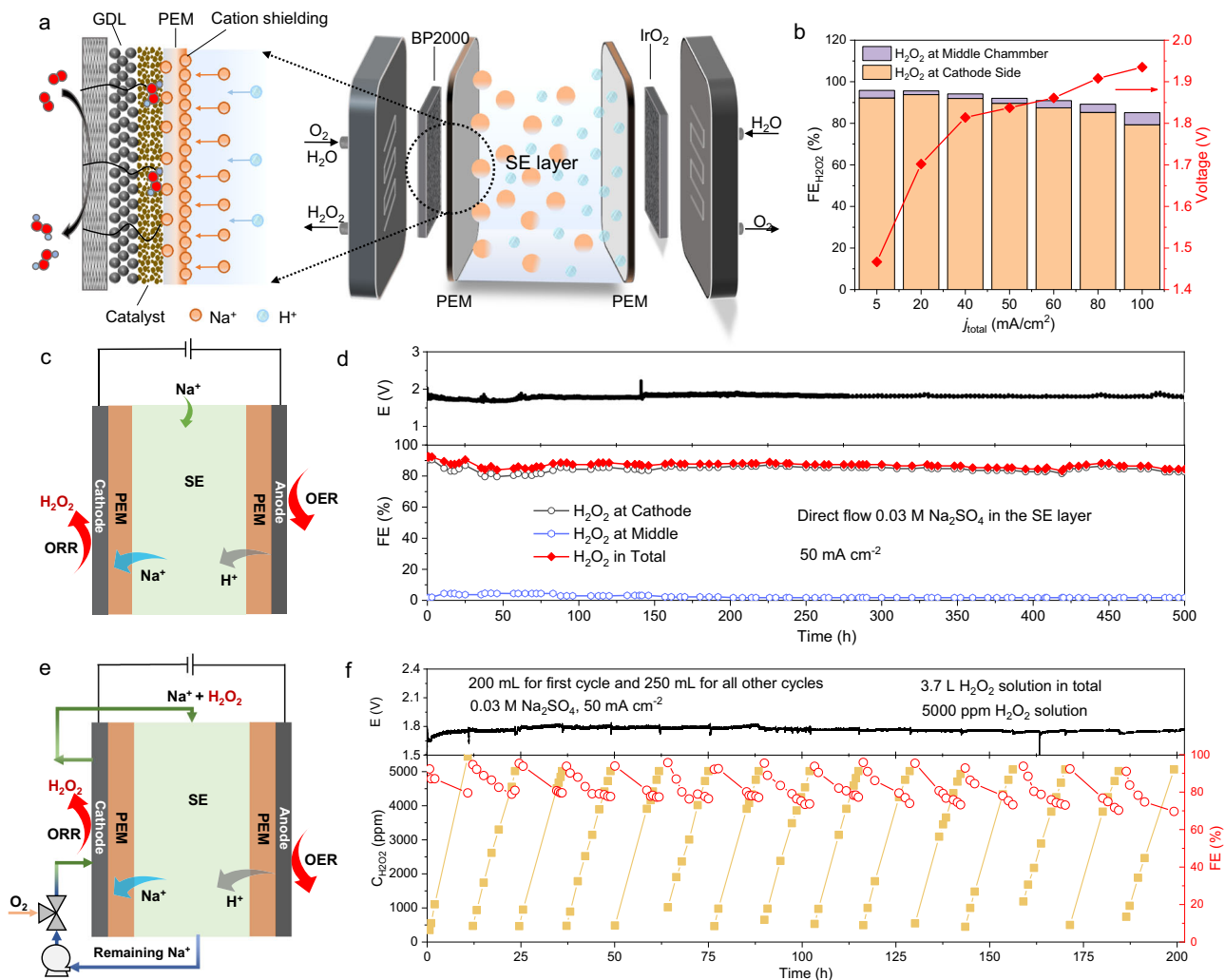
Fig. 6 Continuous production of H_2O_2 solution using carbon catalyst in a SE cell with a double-PEM configuration. a Schematic illustration of reducing O_2 to H_2O_2 in our SE cell with double-PEM configuration. The $O_2 + H_2O$/PEM//SE//PEM/H_2O cell in which O_2 is reduced at the cathode side to form H_2O_2 and flowed out by H_2O flow. The cations in the middle chamber cross over the PEM under an applied reduction potential and move to the cathode, protecting the catalyst surface for the production of H_2O_2. **b** The I–V curve and corresponding FEs for producing H_2O_2 using the SE cell with double-PEM configuration through flowing 0.03 M Na_2SO_4 in the middle chamber. The concentration of Na_2SO_4 can be varied. **c, d** The schematic illustration and chronopotentiometry stability test of the SE cell with double-PEM configuration by directly flowing 0.03 M Na_2SO_4 solution in the middle chamber at 50 mA·cm^{-2} current density. The flow rate of Na_2SO_4 solution is 2.7 mL min^{-1}. The oxygen gas (flow rate 180 sccm) and DI water (flow rate 10.8 mL min^{-1}) are mixed and flowed into the cathode to producing H_2O_2 solution. DI water with flow rate of 2.7 mL min^{-1} was circulated at the anode side. **e, f** The schematic illustration and chronopotentiometry stability test of the SE cell for practically producing 5000 ppm H_2O_2 solution. The volume of Na_2SO_4 stock solution in the first cycle is 200 mL, and the other 14 cycles hold 250 mL. The SE cell can produce around 3.7 L 5000 ppm H_2O_2 solution in 15 cycles for more than 200 h. The liquid flow rate is 4.5 mL min^{-1} and the O_2 gas flow rate is 140 sccm. The total geometric area of the flow field in the cathode of our SE cell is 4 cm^2.

H_2O_2 solution was achieved in 17 h by circulation of the 50 mL water at the cathode side (Fig. S30). Based on the above promising H_2O_2 activity, selectivity and especially the durability, and since all the reactor components, including catalysts, membrane, and the polymer SE are all commercially available, our PEM-based H_2O_2 SE cell with cation promotion effect has a great potential for future's practical applications.

To conclude, we presented a cation-regulated interfacial engineering approach to improve the catalytic performance of O_2 reduction to H_2O_2 at industrial-relevant rates in strong acidic media. By adding a small number of alkali metal cations in acid solutions, the selectivity and stability of H_2O_2 generation using commercial carbon black catalyst can be dramatically improved, especially under large ORR current densities (over 400 mA cm^{-2}). Modeling of reaction and local environment suggest that the cations could preferentially be attracted to the catalyst/electrolyte

interface, showing a "shielding effect" to squeeze out the catalyst/electrolyte interfacial protons and thus prevent further reduction of generated H_2O_2 to water. A double-PEM-based reactor was further developed for continuous production of H_2O_2 solution. By using only 0.03 M Na_2SO_4 as the cation source, a promoted H_2O_2 FE (~90%) and stability (>500 h) were achieved. In light of this performance, this would be a promising demonstration of the use of renewable electricity for the continuous generation of H_2O_2 through O_2 reduction at a more practical scale. This cation "shielding effect" could also be used in other electrocatalytic reactions such as selective CO_2 reduction into fuels and chemicals or N_2 reduction into ammonia.

Experiment

Materials. All chemicals including lithium sulfate (Li_2SO_4), sodium sulfate (Na_2SO_4), potassium sulfate (K_2SO_4), caesium

sulfate (Cs_2SO_4), perchloric acid, sulfuric acid, and Nafion per-fluorinated resin solution (527084-25 mL) were purchased from Sigma Aldrich. H_2O_2 solution (35 wt%) was purchased from Merck & Co. Vulcan XC-72 were purchased from Fuel Cell Store. The conductive carbon black BP2000 was purchased from Cabot Corporation. Millipore water (18.2 MΩ·cm) was used throughout all experiments.

Preparation of electrodes. Typically, 40 mg conductive carbon black (BP2000) and 80 μL of Nafion (527084-25 mL) binder solution was mixed with 4 mL of 2-proponal (Sigma-Aldrich) and 1 ml methanol. After sonication in ice water for 30 min, the obtained homogeneous ink was air-brushed onto a 5×5-cm^2 gas diffusion layer (GDL, Sigracet 28 BC, Fuel Cell Store) electrode at room temperature. Then the prepared electrode was dried in a vacuum at room temperature for 24 h before use. The procedure for preparation electrodes with other catalysts is same as that of carbon black BP2000. The reduced graphene oxide (rGO) catalyst was pretreated using HCl and acetone to remove impurities before making the catalyst ink.

Activation of the Nafion-117 membrane. The proton exchange membrane (PEM, Nafion-117) was purchased from Fuel Cell Store. The Nafion-117 membrane was pre-treated with 5% (v/v) H_2O_2 for 1 h at 80 °C and 10% (v/v) H_2SO_4 for 1 h at 80 °C before assembling a cell.

Materials characterization. The scanning electron microscopy (SEM) was performed on an FEI Quanta 400 field emission scanning electron microscope. BET surface area analysis was performed using Quantachrome Autosorb-iQMP/Kr BET Surface Analyzer.

Electrochemical test in flow cell. The electrochemical H_2O_2 generation was conducted at 25 °C by using a conventional flow cell with a typical three-electrode setup, and the electrochemical response was recorded by using a BioLogic VMP3 workstation. The cathode and IrO_2 anode (Fuel Cell Store) were placed on opposite sides of two 0.5 cm thick PTFE plates with 0.5 cm * 2 cm channels. The catalyst layers faced the flowing liquid electrolyte, and the geometric surface area of the catalyst was 1 cm^2. A Nafion-117 film was sandwiched by the two PTFE plates to separate the chambers. At the cathode side, 30 sccm humidified O_2 was supplied through a titanium gas flow chamber, and a catholyte containing 0.1 M H_2SO_4 and cations flowed into the cathode chamber. The catholyte flow rate of 1.8 mL min^{-1} was controlled by a syringe pump. The pH value of the catholyte was determined by an Orion 320 PerpHecT LogR Meter (Thermo Scientific). At the anode side, 0.1 M H_2SO_4 anolyte was circulated with a flow rate of 1.8 mL min^{-1} for O_2 evolution reaction as the counter electrolyte. A saturated calomel electrode (SCE, CH Instruments) was employed as the reference electrode. All potentials measured against SCE were converted to the reversible hydrogen electrode (RHE) scale using $E_{RHE} = E_{SCE} + 0.241 V + 0.0591 \times pH$. The resistance (Rs) of the catalytic system was determined by potentiostatic electrochemical impedance spectroscopy (PEIS) at frequencies ranging from 0.1 Hz to 200 kHz. All the measured potentials using the three-electrode flow cell setup were manually 85% compensated unless stated otherwise.

Solid state electrolyte cell with double-PEM configuration. The continuous electrosynthesis of H_2O_2 was conducted using a solid electrolyte (SE) cell with a sandwiched double-PEM configuration. The cell configurations and the production setup are illustrated in Fig. 6a and Fig. S25. The cathode side was supplied with an oxygen/water mixture of 180 sccm of O_2 gas and

10.8 mL min^{-1} of DI water. The gas flow rate was controlled by a mass flow meter (MFC) and the water flow rate was controlled by a syringe pump. The flow rate of H_2O_2 product at the outlet was calibrated using a measuring cylinder. The fast water flow in the gas/liquid mixture through the cathode chamber is beneficial for bringing out the generated H_2O_2 molecules and decreasing the further electroreduction of H_2O_2. In the middle chamber, the styrene-divinylbenzene sulfonated copolymer Dowex 50WX8 hydrogen form (Sigma–Aldrich) cation conductor was employed as the SE. A solution containing H_2SO_4 and/or Na_2SO_4 flowed into the SE layer controlled by a syringe pump. The anode side was circulated with 0.1 M H_2SO_4 at 2.7 mL min^{-1}. All the measured potentials using a two-electrode setup were manually 100% compensated unless stated otherwise.

Bath synthesis of 5000 ppm H_2O_2 Solution using double-PEM cell. The bath electrosynthesis of 5000 ppm H_2O_2 was conducted using double-PEM cell configuration (as shown in Figs. 6a and S25). A certain volume of 0.03 M Na_2SO_4 solution (200 mL for the first cycle, and 250 mL for other cycles) was supplied into the middle SE layer with flow rate of 4.5 ml min^{-1}. The outlet of the middle chamber was mixed with 140 sccm O_2 gas and then supplied to the cathode side for producing H_2O_2. The cathode outlet containing H_2O_2 and remaining Na_2SO_4 was then circulated back to the middle SE chamber for continually running of the cell. Once the accumulated H_2O_2 concentration reached around 5000 ppm, the cell was flushed with fresh 0.03 M Na_2SO_4 for 10 min to remove residue H_2O_2, and another bottle of fresh 0.03 M Na_2SO_4 (250 mL) was used to start a new batch.

Determination of the H_2O_2 concentration. The concentration of the generated H_2O_2 was determined through a titration process. After electrolysis, the as-produced H_2O_2 solution was collected and evaluated using the standard potassium permanganate (0.1 N $KMnO_4$ solution, Sigma–Aldrich) titration process, according to the following equation:

$$2MnO_4^- + 5H_2O_2 + 6H^+ \rightarrow 2Mn^{2+} + 5O_2 + 8H_2O \qquad (1)$$
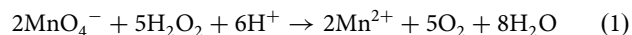
The sulfuric acid (1 M H_2SO_4) was used as the H^+ source. The FE for H_2O_2 production is calculated using the following equation:

$$FE = \frac{\text{generated } H_2O_2 \left(\text{mol L}^{-1}\right) \times 2 \times 96485 \left(\text{C mol}^{-1}\right) \times \text{flow rate (mL s}^{-1})}{j_{total}(mA)}$$
$$\times 100 \text{ (maximum 100\%)}$$
$$(2)$$

Electrochemical H_2O_2 dissociation. The electrochemical H_2O_2 dissociation was conducted in a customized gas-tight H-type glass cell at 25 °C. Before the experiment, the glass cell was carefully cleaned by boiling the cell in a mixture of H_2SO_4: H_2O_2 (3:1) for 1 h. After being thoroughly cleaned by DI at room temperature, the cell was further boiled in DI water for another 1 h to totally remove H_2O_2 residual.

The electrochemical H_2O_2 dissociation was conducted with a BioLogic VMP3 workstation. The cathode electrode was prepared by spray coating carbon black (BP2000) on a GDL (Sigracet 28 BC, Fuel Cell Store), and the anode electrode was a carbon rod. The cathode electrode was fixed using a gold-coated clip and the exposed geometric surface area of each electrode was 1 cm^2. Since the traditional clip made of iron can be easily dissolved to Fe^{2+}/Fe^{3+} by acid and may contribute to the H_2O_2 dissociation, the gold-coated clip is necessary to avoid the dissolution of the iron clip during the process. The working and counter electrodes were parallel and separated by a clean PEM. The mixture of 0.2 M H_2O_2 + 0.1 M H_2SO_4 was used as catholyte, 0.1 M H_2SO_4 was used as anolyte, and

each volume of the electrolyte was 25 mL. A gas dispersion frit was used at the cathode chamber to provide vigorous electrolyte mixing. The cathode chamber was supplied with Ar gas (99.999% Praxair) at a rate of 20 sccm for 30 min before the electrochemical measurements. During electrolysis, continuous Ar flow was supplied throughout the experiment and the gas outlet was connected to a gas chromatograph (GC, Shimadzu GC-2014 GC) for detection of the H_2 gas. The H_2 amount was quantified by a thermal conductivity detector. After the electrochemical decomposition, the amount of H_2O_2 remaining was determined by using the standard potassium permanganate titration process.

Theoretical simulation. The Vienna Ab initio Simulation Package (VASP)[40,41], together with the VASPsol patch[42], was employed to perform slow-growth calculation. The constant potential along the MD track is realized by adjusting the number of electrons on-the-fly, as described in our previous work[35]. Perdew-Burke-Ernzerhof (PBE) functional[43] together with D3 van der Waals correction[44] were employed in most of the calculations. The cutoff energy of the plane-wave basis is 400 eV in the relaxation while 300 eV was used in the MD simulations. Gamma-only MD calculations were done for the thick model in Fig. 5a, b (water layers equivalent to 6 ice layers), while $3 \times 3 \times 1$ Gamma-centered k-mesh was used in MD simulations using the thinner defect-graphene model shown in Fig. S17. One proton is added into the 45 H_2O molecules to simulate the pH = 0 condition. We choose the bond length (*-O or O-OH) to be the reaction coordinate (ε). Time step in MD was set to be 0.5 femtoseconds, and the $\partial\varepsilon$ in slow-growth method[35] was set to be 0.0004 Å. A Nose-Hoover thermostat[45] was used to keep temperature (statistically) constant at 300 K. The proton is determined as the H that is farthest from the central O among two other H atoms of a H_3O^+ for snapshots that are evenly distributed along the AIMD track.

Data availability
The data that support the findings of this study are available from the corresponding authors upon reasonable request.

References
1. https://www.energy.gov/sites/prod/files/2015/08/f26/chemical_bandwidth_report.pdf.
2. Ciriminna, R., Albanese, L., Meneguzzo, F. & Pagliaro, M. Hydrogen peroxide: a key chemical for today's sustainable development. *ChemSusChem* **9**, 3374–3381 (2016).
3. Campos-Martin, J. M., Blanco-Brieva, G. & Fierro, J. L. G. Hydrogen peroxide synthesis: an outlook beyond the anthraquinone process. *Angew. Chem. Int. Ed.* **45**, 6962–6984 (2006).
4. Yang, S. et al. Toward the decentralized electrochemical production of H_2O_2: a focus on the catalysis. *ACS Catal.* **8**, 4064–4081 (2018).
5. Perry, S. C. et al. Electrochemical synthesis of hydrogen peroxide from water and oxygen. *Nat. Rev. Chem.* **3**, 442–458 (2019).
6. Jiang, Y. et al. Selective electrochemical H_2O_2 production through two-electron oxygen. *Electrochem. Adv. Energ. Mater.* **8**, 1801909 (2018).
7. Zhang, X., Xia, Y., Xia, C. & Wang, H. Insights into practical-scale electrochemical H_2O_2 synthesis. *Trends Chem.* **2**, 942–953 (2020).
8. Kim, H. W. et al. Efficient hydrogen peroxide generation using reduced graphene oxide-based oxygen reduction electrocatalysts. *Nat. Catal.* **1**, 282–290 (2018).
9. Lu, Z. et al. High-efficiency oxygen reduction to hydrogen peroxide catalysed by oxidized carbon materials. *Nat. Catal.* **1**, 156–162 (2018).
10. Jung, E. et al. Atomic-level tuning of Co–N–C catalyst for high-performance electrochemical H_2O_2 production. *Nat. Mater.* **19**, 436–442 (2020).
11. Jiang, K. et al. Highly selective oxygen reduction to hydrogen peroxide on transition metal single atom coordination. *Nat. Commun.* **10**, 3997 (2019).
12. Chang, Q. et al. Promoting H_2O_2 production via 2-electron oxygen reduction by coordinating partially oxidized Pd with defect carbon. *Nat. Commun.* **11**, 2178 (2020).
13. Chen, S. et al. Designing boron nitride islands in carbon materials for efficient electrochemical synthesis of hydrogen peroxide. *J. Am. Chem. Soc.* **140**, 7851–7859 (2018).
14. Han, G.-F. et al. Building and identifying highly active oxygenated groups in carbon materials for oxygen reduction to H_2O_2. *Nat. Commun.* **11**, 2209 (2020).
15. Tang, C. et al. Coordination tunes selectivity: two-electron oxygen reduction on high-loading molybdenum single-atom catalysts. *Angew. Chem. Int. Ed.* **59**, 9171–9176 (2020).
16. Chen, S. et al. Chemical identification of catalytically active sites on oxygen-doped carbon nanosheet to decipher the high activity for electro-synthesis hydrogen peroxide. *Angew. Chem. Int. Ed.* **60**, 16607–16614 (2021).
17. Chen, Z. et al. Development of a reactor with carbon catalysts for modular-scale, low-cost electrochemical generation of H_2O_2. *React. Chem. Eng.* **2**, 239–245 (2017).
18. Li, X. et al. Molecule confined isolated metal sites enable the electrocatalytic synthesis of hydrogen peroxide. *Adv. Mater.*, **2021**, 2104891.
19. Qiang, Z., Chang, J.-H. & Huang, C.-P. Electrochemical generation of hydrogen peroxide from dissolved oxygen in acidic solutions. *Water Res.* **36**, 85–94 (2002).
20. Pulidindi, K. & Pandey, H. Hydrogen peroxide market size by end-user Industry (Paper & Pulp, Chemical, Waste Water Treatment, Mining), Industry Analysis Report, Regional Outlook, Application Potential, Price Trends, Competitive Market Share & Forecast, 2020–2026, https://www.gminsights.com/industry-analysis/hydrogen-peroxide-market (2016).
21. Yang, S., Tak, Y. J., Kim, J., Soon, A. & Lee, H. Support effects in single-atom platinum catalysts for electrochemical oxygen reduction. *ACS Catal.* **7**, 1301–1307 (2017).
22. Verdaguer-Casadevall, A. et al. Trends in the electrochemical synthesis of H_2O_2: enhancing activity and selectivity by electrocatalytic site engineering. *Nano Lett.* **14**, 1603–1608 (2014).
23. Siahrostami, S. et al. Enabling direct H_2O_2 production through rational electrocatalyst design. *Nat. Mater.* **12**, 1377–1143. (2013).
24. Shen, R. et al. High-concentration single atomic Pt sites on hollow CuSx for selective O_2 reduction to H_2O_2 in acid solution. *Chem* **5**, 2099–2110 (2019).
25. Dong, K. et al. Noble-metal-free electrocatalysts toward H_2O_2 production. *J. Mater. Chem. A* **8**, 23123–23141 (2020).
26. Gao, J. et al. Enabling direct H_2O_2 production in acidic media through rational design of transition metal single atom catalyst. *Chem.* **6**, 658–674 (2020).
27. Sun, Y. et al. Activity–selectivity trends in the electrochemical production of hydrogen peroxide over single-site metal–nitrogen–carbon catalysts. *J. Am. Chem. Soc.* **141**, 12372–12381 (2019).
28. Zhang, Q. et al. Direct insights into the role of epoxy groups on cobalt sites for acidic H_2O_2 production. *Nat. Commun.* **11**, 4181 (2020).
29. Iglesias, D. et al. N-Doped graphitized carbon nanohorns as a forefront electrocatalyst in highly selective O_2 reduction to H_2O_2. *Chem.* **4**, 106–123 (2018).
30. Melchionna, M., Fornasiero, P. & Prato, M. The rise of hydrogen peroxide as the main product by metal-free catalysis in oxygen reductions. *Adv. Mater.* **31**, 1802920 (2019).
31. Yamanaka, I., Hashimoto, T., Ichihashi, R. & Otsuka, K. Direct synthesis of H_2O_2 acid solutions on carbon cathode prepared from activated carbon and vapor-growing-carbon-fiber by a H_2/O_2 fuel cell. *Electrochim. Acta* **53**, 4824–4832 (2008).
32. Kolyagin, G. A. & Kornienko, V. L. Effect of trialkylammonium salts and current density on the electrosynthesis of hydrogen peroxide from oxygen in a gas-diffusion electrode in acid solutions. *Russ. J. Appl. Chem.* **79**, 746–751 (2006).
33. Kolyagin, G. A. & Kornienko, V. L. Kinetics of hydrogen peroxide accumulation in electrosynthesis from oxygen in gas-diffusion electrode in acidic and alkaline solutions. *Russ. J. Appl. Chem.* **76**, 1070–1075 (2003).
34. Huang, J. E., Li, F., Ozden, A. & Rasouli, A. S. CO_2 electrolysis to multicarbon products in strong acid. *Science* **372**, 1074–1078 (2021).
35. Zhao, X. & Liu, Y. Origin of selective production of hydrogen peroxide by electrochemical oxygen reduction. *J. Am. Chem. Soc.* **143**, 9423–9428 (2021).
36. Zhao, X. & Liu, Y. Unveiling the active structure of single Nickel atom catalysis: critical roles of charge capacity and hydrogen bonding. *J. Am. Chem. Soc.* **142**, 5773–5777 (2020).
37. Li, H. et al. Scalable neutral H_2O_2 electrosynthesis by platinum diphosphide nanocrystals by regulating oxygen reduction reaction pathways. *Nat. Commun.* **11**, 3928 (2020).
38. Xia, C., Xia, Y., Zhu, P., Fan, L. & Wang, H. Direct electrosynthesis of pure aqueous H_2O_2 solutions up to 20% by weight using a solid electrolyte. *Science* **366**, 226–231 (2019).

39. Xia, C. et al. Continuous production of pure liquid fuel solutions via electrocatalytic CO_2 reduction using solid-electrolyte devices. *Nat. Energy* **4**, 776–785 (2019).

40. Kresse, G. & Furthmüller, J. Efficiency of *ab*-initio total energy calculations for metals and semiconductors using a plane-wave basis set. *Comput. Mater. Sci.* **6**, 15–50 (1996).

41. Kresse, G. & Hafner, J. Ab initio molecular dynamics for liquid metals. *Phys. Rev. B* **47**, 558–561 (1993).

42. Mathew, K., Kolluru, V. S. C., Mula, S., Steinmann, S. N. & Hennig, R. G. Implicit self-consistent electrolyte model in plane-wave density-functional theory. *J. Chem. Phys.* **151**, 234101 (2019).

43. Ernzerhof, M. & Perdew, J. P. Generalized gradient approximation to the angle- and system-averaged exchange hole. *J. Chem. Phys.* **109**, 3313–3320 (1998).

44. Grimme, S., Antony, J., Ehrlich, S. & Krieg, H. A consistent and accurate ab initio parametrization of density functional dispersion correction (DFT-D) for the 94 elements H-Pu. *J. Chem. Phys.* **132**, 154104 (2010).

45. Hoover, W. G. Canonical dynamics: equilibrium phase-space distributions. *Phys. Rev. A* **31**, 1695–1697 (1985).

Acknowledgements

Author contributions

X.Z. and X.H.Z. contributed equally. X.Z. and H.W. conceived the project and designed the experiments. X.Z., P.Z., Z.A., and Z.W. perform the experimental study. X.H.Z. and Y.L. performed the theoretical study. X.Z., X.H.Z., Y.L., and H.W. wrote the manuscript with support from all authors.

Competing interests

A patent application has been filed based on this study.

Additional information

Supplementary information The online version contains supplementary material available at https://doi.org/10.1038/s41467-022-30337-0.

Correspondence and requests for materials should be addressed to Xiao Zhang, Yuanyue Liu or Haotian Wang.

Peer review information *Nature Communications* thanks Sungeun Yang, Jeng-Han Wang and the other anonymous reviewer(s) for their contribution to the peer review of this work. Peer review reports are available.

Reprints and permission information is available at http://www.nature.com/reprints

Publisher's note Springer Nature remains neutral with regard to jurisdictional claims in published maps and institutional affiliations.